

Principal correlation decomposition of experimental and numerical data for observable diagnosis

B. Lyu¹†

¹State Key Laboratory for Turbulence and Complex Systems, College of Engineering, Peking University, Beijing 100871, China

(Received xx; revised xx; accepted xx)

A method, referred to as the principal correlation decomposition (PCD), is proposed in this paper to optimally dissect complex flows into mutually orthogonal modes that are ranked by their correlated energy with an observable. It is particularly suitable for identifying the observable-correlated flow structures, while effectively excluding those uncorrelated even though they may be highly energetic. Therefore, this method is capable of extracting coherent flow features under very low signal-to-noise ratio (SNR). A numerical validation is conducted and shows that the new method can robustly identify the observable-correlated flow events even though the underlying signal is corrupted by random noise that is four orders of magnitude more energetic. Moreover, the resolution continues to improve if the flow is sampled for a longer duration, which is often readily available in experimental measurements. This method is subsequently used to analyse the unsteady vortex shedding from a cylinder and a subsonic turbulent jet. This new decomposition represents a data-driven method of effective order-reduction for highly noisy experimental and numerical data and is very effective in identifying the source and descendent events of a given observable. It is expected to find wide applications in flow observable diagnosis and its control such as noise control.

1. Introduction

Many flows in nature are of a complex nature, such as a boundary layer formed over a sand dune or compressed air inside an aeroengine. This is particularly true at high Reynolds numbers, where most realistic engineering flows occurs, because turbulence comes into play showing a wide range of temporal and spatial scales. To understand, model and possibly exert control on these flows, it is crucial to extract dominant structures and reduce the degrees of freedom of the flow.

Extensive research has been conducted to extract coherent features and decompose complex flows into a collection of simpler modes. Well-established methods include for instance Proper Orthogonal Decomposition (POD), Dynamic Mode Decomposition

† Email address for correspondence: b.lyu@pku.edu.cn

(DMD), resolvent analysis and input-output analysis (Taira et al. 2017). Among these, POD and DMD fall into the category of data-driven approach, while the resolvent analysis and input-output analysis are model-based.

POD (Lumley 1967; Berkooz et al. 1993) is a particularly well-known data-driven method and represents a powerful tool of feature extraction and order reduction. The essence of POD is to decompose a complex flow into mutually orthogonal modes. These modes are ranked by their fluctuation energy defined using appropriate norms. If the total flow is comprised of a few energetic coherent structures, they can be effectively identified as the leading-order modes of the flow by POD. A linear combination of these leading-order modes then forms an optimal reduced-order representation of the total flow. POD may be used to extract the spatial or temporal structures, using the so-called classical (Lumley 1970) and snapshot POD (Sirovich 1987), respectively. These two structures are coupled, in the sense that the temporal structures represents the temporal variation of its corresponding spatial mode, while the spatial mode represents the spatial distribution of its corresponding temporal mode (Aubry 1991). This leads to the so-called Bi-orthogonal Decomposition (BOD). Recent years have also seen the increasingly widely-used Spectral Proper Orthogonal Decomposition (SPO) in studying turbulent flows (Towne et al. 2018). It is worth noting that since POD rely on the existing underlying coherence within the flow, it is capable of identifying the flow structures that are dynamically nonlinear compared to linear model-based approaches shown in the rest of this paper.

While POD aims to identify the coherent structures within a complex flow, DMD aims to extract temporal evolutionary information of the underlying dynamics captured in the data (Schmid 2010). The resulting representation is a dynamical system of fewer degrees of freedom. The DMD starts by assuming a linear mapping between a sequence of the flow data, and the dynamics are extracted by examining the eigenvalues of a similarity matrix. For a linear system, this amounts to identify the eigen-modes of the system. For nonlinear system, DMD is connected with the modes of the so-called Koopman operator (Schmid 2022). Unlike POD, DMD modes are ranked by their “contribution” to the overall dynamics embedded in the data sequence. Recent years have seen numerous variants of DMD such as the extended DMD (Williams et al. 2015) and Residual DMD (Colbrook et al. 2023). More details on the recent development of DMD can be found from the recent review by Schmid (2022).

As mentioned above, both POD and DMD are data-driven, while the resolvent analysis is based on the modal analysis of a linear operator. The resolvent analysis has an early origin in control theory and is based on the pseudospectrum of an operator (Trefethen et al. 1993), rather than the spectrum. For example, when the flow is decomposed into a base and fluctuations parts, the Navier-Stokes equations can be rewritten and interpreted as a linear system governing the evolution of the flow perturbations. The nonlinear terms are collected on the right hand side and interpreted as the forcing of the system.

The resolvent modes are ranked by the energy gain between the response and forcing. Therefore, the resolvent analysis examines the gains properties of the linearized operator, and has been used to study turbulence from a linearized Navier-Stokes equation point of view (Farrell and Ioannou 1993; Mckeon 2010). Recent studies also show that the leading-order resolvent modes match with the leading-order POD modes extracted from a numerically simulated high-speed jets (Schmidt et al. 2018). Input-Output analysis (Jovanović 2021) is similar to resolvent analysis in that a modal analysis is performed on a linearized operator. Input-Output analysis differs from the conventional resolvent analysis in that a weight maybe added to the operator to bias the both the forcing and response towards interested domain or observables (Jeun et al. 2016). Therefore, input-output analysis may be regarded as a weighted resolvent analysis.

POD and DMD, together with their variants, are common flow decomposition methods used in fluid mechanics. These provide important tools of probing the structures and dynamics of an underlying dynamical system. The ultimate goal of identifying the dominant structures or dynamics is, however, often to understand and possibly control some observables of the flow, such as to reduce the drag of a cylinder, minimize the unsteady force of a wing, or abate the noise emission from a jet. However, because POD modes are ranked by their fluctuation energy, the leading-order modes are not necessarily the most important structures as far as the observable is concerned, although they do carry the largest energy. For example, a large coherent structure effectively extracted from a turbulent jet using POD may be very inefficient at generating noise. In other words, the leading-order POD mode may not be the leading-order noise-generating flow structure. For example, it has been shown that a substantial number of near-field POD modes are required for reconstructing the acoustic field (Freund and Colonius 2009). Similarly, DMD extracts the dominant dynamics embedded within the flow without taking their connection with any observable into account. Consequently, the leading-order dynamic mode does not necessarily represent the flow events that reflect the dynamics of the observables.

That the energy rank may not be an appropriate measure, in particular for an observable-related diagnosis, is a well-recognized limitation of POD (Schmid 2010). One widely-used solution to overcome this difficulty is to use different norms to bias the decomposition towards interested observables. For example, Freund and Colonius (2009) performed the POD decomposition of a turbulent jet using various norms including the near-field turbulent kinetic energy, near-field pressure and far-field pressure. When the far-field pressure norm is used, the near-field flow quantities drop out in the correlation matrix and the resulting spectrum is effectively ranked only by the far-field pressure. Although the near-field flow can still be project onto the far-field basis, the resulting near-filed mode does not necessarily form a direct continuation of the far-field physics, particularly when the near- and far-field exhibit completely different dynamics.

On the other hand, the resolvent analysis and input-output analysis decompose the

flow to maximize the energy gain between the output and forcing based on the spectral theory of linear operators, and the observable may be directly included in the choice of output. However, a known operator describing the underlying system is often needed, but may not be readily known in many cases. Furthermore, a linearized operator may not be an appropriate representation of the dynamical system, particularly in highly nonlinear systems. For example, a recent input-output analysis was performed on compressible subsonic and supersonic jets, and found that a considerable number of modes were required to reconstruct the acoustic energy of subsonic jets (Jeun et al. 2016), which may be partly due to the limitation imposed by linearity.

In this paper, we aim to develop a new flow decomposition method that is suitable for observable diagnosis based on flow and observable snapshots without relying on linear operators. Instead of redefining the POD energy norm to bias towards the observable, the decomposition aims to introduce a rank based on a correlation norm between the resulting modes and the observable, hence including both the flow and observable data in the correlation matrix. This paper is structured as follows, section 2 shows a mathematical formulation of the new method, including its validations. The following section applies this new technique to both experimental and numerical data. The following section concludes the paper and lists some future work.

2. The principal correlation decomposition

2.1. The decomposition procedure

Assume that we have a sequence of snapshots \mathbf{u}_i obtained by sampling a flow field $u(t, \mathbf{x})$ at time t_i , where \mathbf{x} represents the coordinates of the flow domain and i is an integer and takes the value of $1, 2, 3 \dots N$, as shown in figure 1. Each snapshot of this sequence is obtained by discretizing the spatial domain on a mesh and represented by a row vector of length M . We write this sequence compactly in a matrix notation as

$$\mathbf{U} = [\mathbf{u}_1, \mathbf{u}_2, \mathbf{u}_3 \dots \mathbf{u}_N]^T. \quad (2.1)$$

Similarly, the sequence of p_i , where i is an integer that takes the values of $1, 2, \dots N+Q-1$ and Q is a positive integer, is obtained by sampling an interested observable $p(t)$ at time $t_i + \tau_d$, where τ_d is a constant representing the time delay between the sampling time of p and u , respectively. Note that the sequence p_i is longer than that of \mathbf{u}_i by $Q-1$ and starts at an earlier or later time of $t_1 + \tau_d$, depending on whether τ_d is a negative or positive value, respectively. This is important and we will discuss its significance in the rest of the paper. We then define the row vectors \mathbf{p}_j as

$$\mathbf{p}_j = [p_j, p_{j+1}, \dots, p_{j+N-1}], \quad (2.2)$$

where j is an integer and $j = 1, 2, \dots, Q-1, Q$. We form a matrix \mathbf{P} such that

$$\mathbf{P} = [\mathbf{p}_1, \mathbf{p}_2, \dots, \mathbf{p}_{Q-1}, \mathbf{p}_Q]^T. \quad (2.3)$$

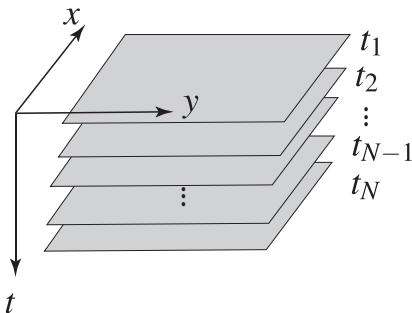


Figure 1: The schematic illustration of the flow snapshots sampled at time t_i , $i = 1, 2, 3 \dots N$. Each snapshot contains data in both x and y directions.

The key step is to construct the correlation matrix \mathbf{A} such that

$$\mathbf{A} = \frac{1}{N\sqrt{Q}}\mathbf{P}\mathbf{U}. \quad (2.4)$$

We then perform the standard Singular Value Decomposition (SVD) of matrix \mathbf{A} , such that

$$\mathbf{A} = \mathbf{W}\mathbf{\Sigma}\mathbf{V}^T, \quad (2.5)$$

where \mathbf{R} and \mathbf{V} are $Q \times Q$ and $M \times M$ unitary matrices respectively, while $\mathbf{\Sigma}$ is a diagonal matrix of $Q \times M$ with the singular values σ_j ($j = 1, 2, 3 \dots, \min(M, Q)$) as its diagonal elements. The column vectors of \mathbf{V} represent the PCD modes of the flow field \mathbf{u}_i , while those of \mathbf{R} represent the cross-correlation functions between the PCD modes and the observable, as will be discussed in detail in section 2.2. From standard SVD, it can be readily shown that these modes are mutually orthonormal and form a complete basis of \mathbb{R}^N . Therefore, the flow field \mathbf{u}_i can be conveniently decomposed as

$$\mathbf{u}_i = \sum_{k=1}^N a_k(t_i)\mathbf{v}_k \quad (2.6)$$

where \mathbf{v}_k denotes the k -th column of \mathbf{V} while $a_k(t_i)$ denotes its corresponding expansion coefficient at time t_i , or equivalently,

$$u(t, \mathbf{x}) = \sum_{k=1}^N a_k(t)\phi_k(\mathbf{x}), \quad (2.7)$$

where $\phi_k(\mathbf{x})$ denote the basis function corresponding to \mathbf{v}_k , while $a_k(t)$ is the expansion coefficient of $u(t, \mathbf{x})$ using the basis $\phi_k(\mathbf{x})$. As shown in section 2.2, these modes are ranked by their correlation with the observable, and a significant order reduction may be expected if only a number of modes are pronouncedly correlated with the observable. Because the correlation plays an essential role in the method, in the rest of this paper it will be referred to as the principal correlation decomposition (PCD).

2.2. Physical significance of PCD modes

The PCD represents an optimal decomposition that maximizes the correlation between the flow field u and the observable p . This can be shown mathematically as follows. Assuming the flow field is described by the function $u(t, \mathbf{x})$ while the observable by $p(t + \Delta t)$, where Δt represents the time shift between flow and the observable. We form the cross-correlation $R(\tau, \mathbf{x})$ using

$$R(\Delta t, \mathbf{x}) = \overline{p(t + \Delta t)u(t, \mathbf{x})}, \quad (2.8)$$

where the bar represents the temporal or ensemble average. In the later case, the statistical processes involved in u and p are assumed to be statistically stationary. Note that in this case it may be replaced by a temporal average if the statistical processes are ergodic. For non-stationary processes, (2.8) explicitly depends on t but the following derivation can still proceed.

Suppose we wish to find a function $\phi(\mathbf{x})$ of unit L_2 norm, such that the inner-product between ϕ and R , defined by

$$R_\phi(\Delta t) = \int_{\Omega} R(\Delta t, \mathbf{x})\phi(\mathbf{x}) dx^n, \quad (2.9)$$

obtains its maximal value in the L_2 norm, where n represent the dimension of the flow field in its domain of definition Ω . Mathematically, this is to equivalent to find a $\phi(\mathbf{x})$ to obtain

$$\max_{\|\phi(\mathbf{x})\|=1} \|R_\phi(\Delta t)\|, \quad (2.10)$$

where $\|\cdot\|$ represents the L_2 norm.

Physically, this is equivalent to find the optimal function ϕ that most correlates with the observable. This is because the ensemble average in (2.8) commutes with the inner product, i.e.

$$R_\phi(\Delta t) = \overline{p(t + \Delta t)a_\phi(t)}, \quad (2.11)$$

where $a_\phi(t)$ represents the expansion coefficient of the flow field u using the basis ϕ , i.e.

$$a_\phi(t) = \int_{\Omega} u(t, \mathbf{x})\phi(\mathbf{x}) dx^n. \quad (2.12)$$

Clearly, we see from (2.11) and 2.12 that R_ϕ represents the cross-correlation between the ϕ mode of the flow and the observable. The L_2 norm of R_ϕ defined over the interval $[0, T]$ is a natural measure of this cross-correlation. We therefore define the correlation energy C_e as the average of $\|R_\phi\|^2$, i.e.

$$C_e = \frac{1}{T} \int_{\tau}^{\tau+T} R_\phi^2(\Delta t) d\Delta t. \quad (2.13)$$

Evidently, if $\phi(\mathbf{x})$ maximizes C_e , it represents a flow structure that most correlates with the observable p .

When the flow field and the observable are discretized both temporally and spatially,

we can show that the matrix \mathbf{A} defined in section 2.1 is identical to $R(\Delta t, \mathbf{x})$ subject to a normalization coefficient $1/\sqrt{Q}$. It is straightforward to show that the SVD of \mathbf{A} yields an optimal orthogonal basis under which the C_e is maximized. The column vectors of \mathbf{V} are these optimal modes, while the corresponding column vectors of \mathbf{R} are the cross-correlation functions. In addition, the squares of the singular values, i.e. σ_j^2 , are precisely the correlation energy C_e between the PCD modes and observable. In particular, when the components of p that correlate with their corresponding PCD modes of u are of equal energy, σ_j^2 also represent the correlated energy of their corresponding PCD modes, and the correlation ranking is identical to the ranking of the observable-correlated flow energy. In summary, instead of decomposing the flow field u based on its energy ranking using the classical Proper Orthogonal Decomposition (POD), (2.5) yields a new type of decomposition that is based on correlation ranking, or the observable-correlated energy ranking in the special case where the correlated components of p are of equal energy.

PCD possesses a number of key advantages that would render it particularly useful for targeted flow diagnosis. First, the decomposition modes are not ranked by their energy, but by the correlated energy with the observable. Flow features that are uncorrelated with the observable can be effectively removed while those correlated are promoted based on the correlation energy. This targets exclusively at the observable and is therefore very useful in diagnosing the sources or descendent structures of the observable. Second, as will be shown in section 2.3, the new decomposition is significantly robust when the signal-to-noise ratio (SNR) is low. This is particularly useful when only a small portion of the flow energy is responsible for the observable, for example in the classical problem of aeroacoustic emission of turbulence. Moreover, this robustness can be continuously improved when a longer time duration is used. This is particularly suitable for experimental diagnosis, where an arbitrarily long measurement can be readily performed. Third, the decomposition would be more capable of order or dimensionality reduction compared to POD. This is because PCD aims to decompose the flow only in the observable-correlated subspace, rather than the entire \mathbb{R}^N . For example, when weak coherent structures in the flow field $u(t, \mathbf{x})$ are heavily polluted by strong random noises, POD would yield a virtually flat spectrum, but the PCD can effectively extract these structures if they are correlated with the observable and the resulting spectrum is of a particularly low order. Last but not the least, PCD is capable of dealing with a very large flow domain, largely because the frequency resolution can be conveniently adjusted by changing Q . For example, by choosing an appropriate frequency resolution, PCD can easily handle the decomposition of a flow field that has up to 10^8 degrees of freedom.

2.3. Validation

To validate that PCD can effectively extract flow events that correlate with an observable, even under very low SNR, we create an artificial one-dimensional unsteady

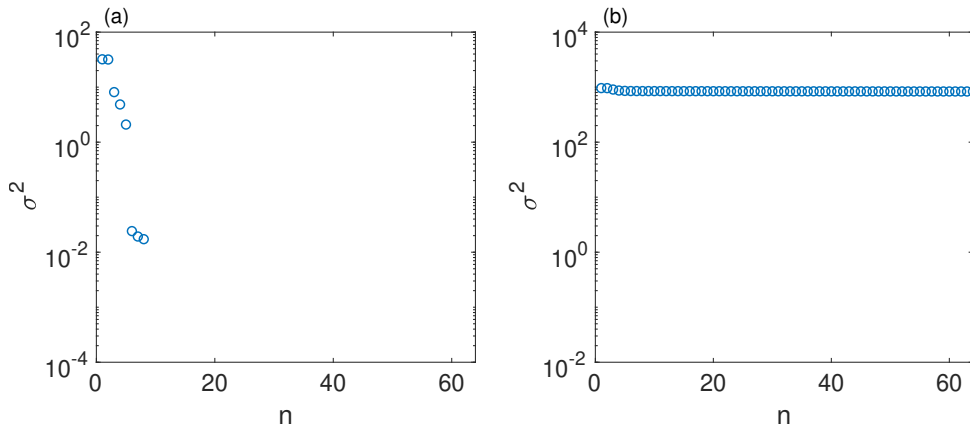


Figure 2: Comparison of the spectra of PCD (a) and POD (b) when the sample duration $N = 10^4$ at a SNR $< 10^{-4}$. PCD is capable of effectively extracting the observable-correlated events leading to a low-rank spectrum while POD results in a flat spectrum.

flow field

$$u(x, t) = 2 \cos(t - x) + 1.5 \cos(2t) \cos(2x) + \cos(3t) \cos(3x) + 0.5 \cos(4t) \cos(4x) + \cos(6t) \cos(6x) \exp(-0.1(x - \pi)^2) + 100r(t, x); \quad (2.14)$$

where $r(t, x)$ represents a random noise field with a uniform probability distribution over $[-0.5, 0.5]$, while other terms represent given flow structures with different amplitudes. Note that the energy of the random noise field is deliberately chosen to be 10^4 stronger than the defined flow structures. Suppose that the observable p is generated by the flow events represented by the first, third, fourth and fifth terms in (2.16), but not by the second and last terms. For instance, p may be given by

$$p(t) = \cos\left(t - \frac{\pi}{4}\right) + \sin\left(3t - \frac{\pi}{3}\right) + \cos(4t) + \cos\left(6t - \frac{\pi}{12}\right), \quad (2.15)$$

where the amplitudes of the terms shown in (2.15) are chosen to be identical, although they may be changed arbitrarily.

Suppose that the flow field u is sampled over $[0, 2N\pi]$ at a sample frequency of $f_s = 128/2\pi$, where N is an integer that can vary. Given the strong random noise used (2.14), N is chosen to be a large number. However, as show in the rest of this paper, this is not necessary when weaker noise is present. p on the other hand is sampled at the same sample frequency but for a slightly longer duration of $2(N + 1)\pi$. At each snapshot, the flow field is discretized on a mesh of 128 points uniformly distributed between $[0, 2\pi]$. Following the procedures introduced in section 2.1, both matrix \mathbf{U} and \mathbf{P} can be easily constructed, where \mathbf{U} is of a size of $128N \times 128$ while \mathbf{P} is of a size $128 \times 128N$. Upon constructing the matrix \mathbf{A} , the PCD can be carried out in a straightforward manner. The resulting PCD spectrum is shown in figure 2(a). To facilitate a direct comparison, the POD spectrum is also shown in figure 2(b).

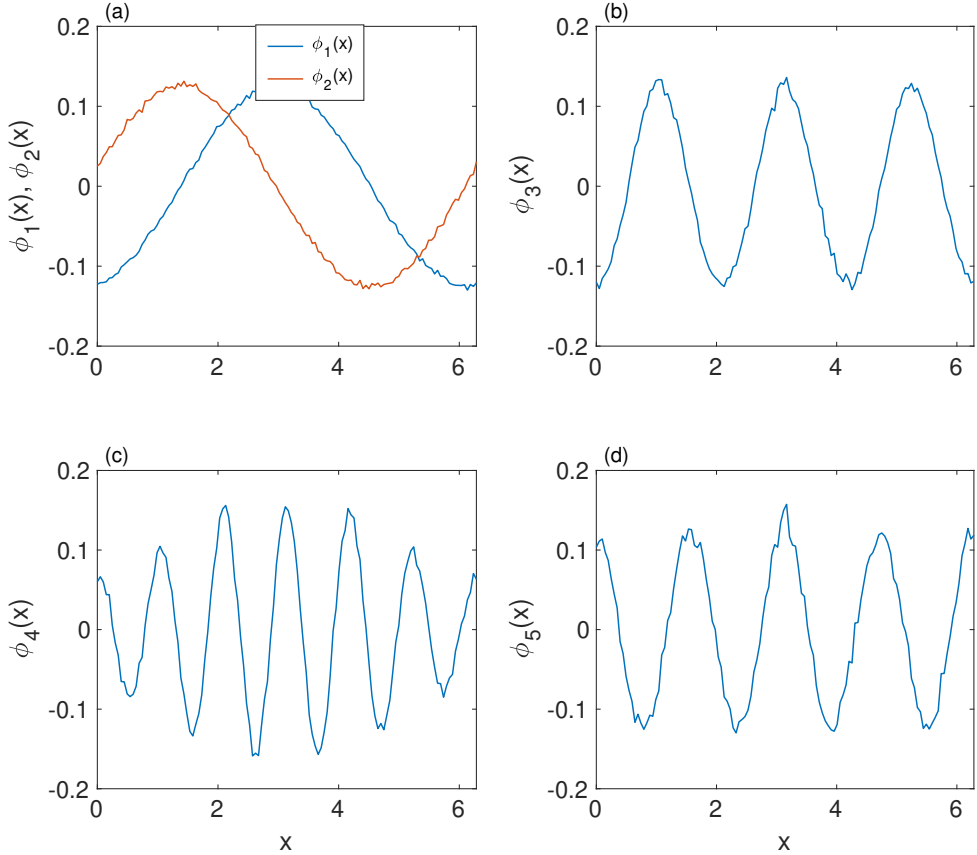


Figure 3: The extracted PCD modes at $N = 10^4$ that correlated most with the observable p corresponding to the first, third, fifth and fourth terms in (2.15), respectively.

Figure 2 shows the PCD spectrum with a desired low-rank behaviour. From figure 2(a) we see that the five modes that correlate with the observable can be robustly identified, even the energy of the random noise is 10^4 stronger. Specifically, the first two equal singular values corresponding to the flow event of the travelling-wave nature, $\cos(t - x)$, i.e. one mode corresponds to $\sin(t + \phi) \sin(x + \phi)$ while the other $\cos(t + \phi) \cos(x + \phi)$ (ϕ is an arbitrary phase delay), as shown in figure 3(a). The third, fourth and fifth singular values correspond to the flow events described by the third, fifth and fourth terms in (2.14), respectively. These can be confirmed by examining the corresponding mode vectors shown in figure 3(c-d). Most importantly, the $\cos(2x)$ mode, which does not correlate with the observable, is robustly removed in the PCD spectrum. This shows that PCD can effectively remove those uncorrelated flow events while only keeping those correlated, and therefore works well for an observable-targeted order reduction. The sixth to the ninth singular values shown in figure 2(a), which are two orders of magnitude weaker than the first few modes, are artefacts introduced by the strong random noise. Note, however, these unphysical modes can be further suppressed robustly if the flow

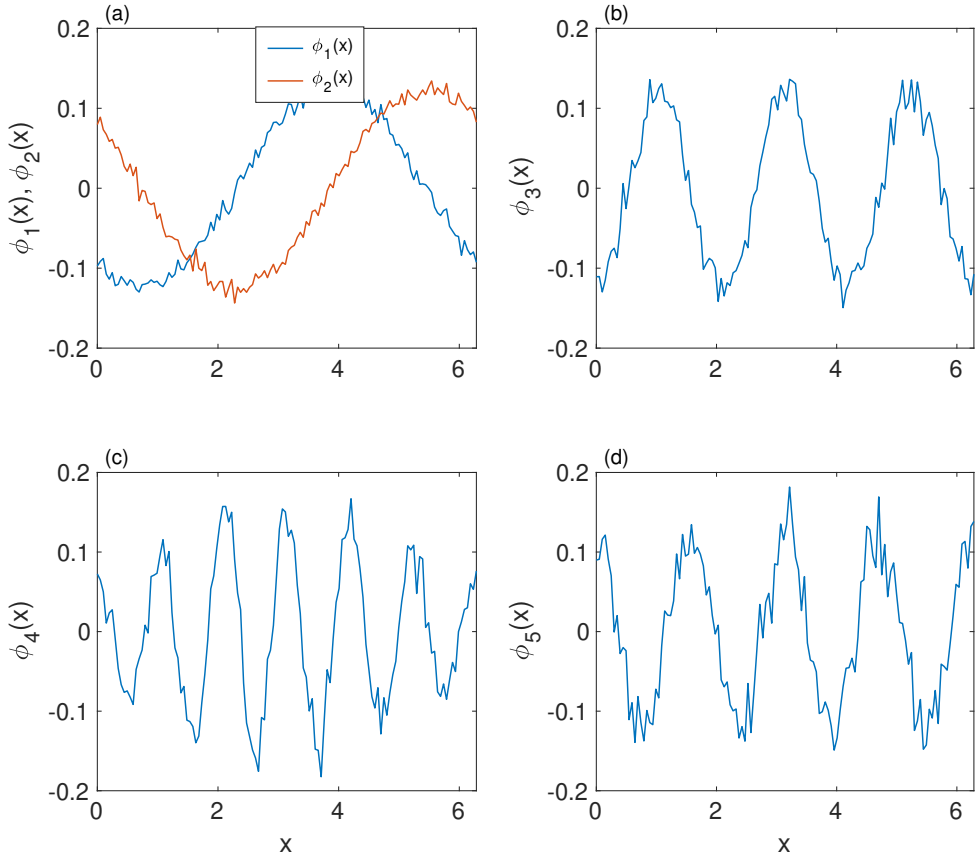


Figure 4: The extracted PCD modes at a SNR of $< 10^4$ when $N = 1000$. Convergence level is reduced compared to figure 3 but the PCD modes are still very clearly identified.

field is sampled for a longer duration (larger N). All other singular values are below 10^{-14} and therefore not shown within the given range. As discussed in section 2.2, the singular values are determined by the correlation energy between corresponding PCD modes and the observable. In this illustrative case, the observable is comprised of four modes of equal amplitude, as shown in (2.15), therefore the singular values in figure 2(a) are precisely the observable-correlated fluctuation energy (subject to a fixed constant), as shown in (2.14).

Figure 3 shows that the extracted modes are subject to small random noise. However, this improves rapidly with the increases of N for the fixed given SNR. In figure 2 and 3, N is taken to be 10000. This is a large number because we deliberately chose a SNR that is as low as 10^{-4} . A small N can also be used at the expense of augmented noise in the resolved modes. For example, figures 4 and 5 show the extracted PCD modes when $N = 1000$ and $N = 100$, respectively. Clearly, we see that using a duration of $N = 1000$ results in PCD modes that converge less well but are still unambiguously identified. When N is reduced to 100, the resolved PCD modes are further corrupted

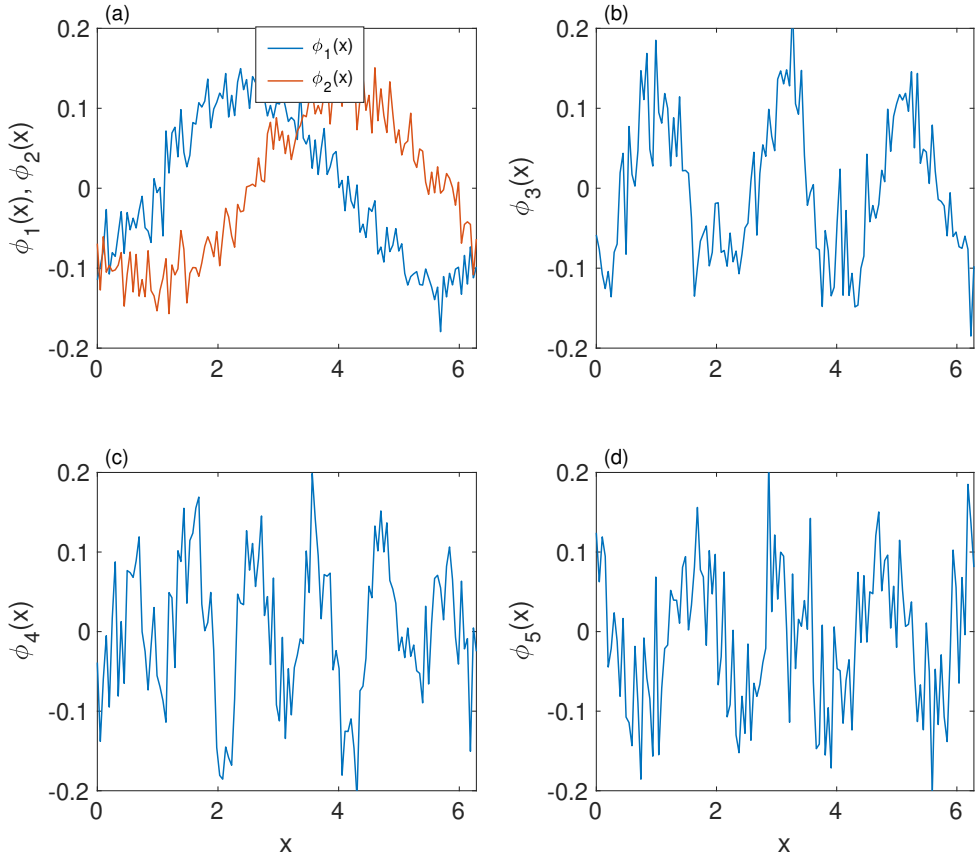


Figure 5: The extracted PCD modes at a SNR of $< 10^4$ when $N = 100$. Convergence level is further reduced compared to figure 4 and the PCD modes can still be identified but with stronger noise corruption.

by the random noise, nevertheless the structures of the modes can still be recognized. Note N here denotes the period of the underlying flow event. At the lowest frequency of 100 Hz widely used in the literature, $N = 100$ yields a sampling duration of 1 s. In the experiments, a record of 100 s can be easily managed.

Figure 5 shows that the PCD modes are corrupted significantly by random noise at a SNR $< 10^{-4}$ when $N = 100$. However, when the random noise is only two orders of magnitude more energetic, $N = 100$ yields sufficiently well-resolved PCD modes. In general, we find that to obtain the same level of convergence, N scales roughly as $1/\text{SNR}$. Conversely, if longer samples are readily available, PCD can robustly extract the observable-correlated flow events at the same level of convergence at an even lower SNR. Therefore, PCD is especially suitable for analysing data acquired in experiments, where the data may be recorded for as long as desired. One application that PCD would be particularly suitable is aeroacoustic source diagnosis because of its lower SNR, since it

is well-established that only a very small portion of unsteady flow energy propagates as acoustic waves, while other strong turbulent fluctuations may be totally silent.

On the other hand, figure 2(b) shows that due to the strong random noise the POD spectrum is completely corrupted and shown as a flat line. The low-rank behaviour embedded within the data therefore cannot be identified. This is expected, because POD modes are ranked by their corresponding fluctuation energy. The random noise present in the flow field is 10^4 stronger than the observable-correlated events, and therefore completely dominate the POD spectrum. More importantly, even though POD may be able to extract the coherent structures when weaker noise is present, it cannot separate the observable-correlated flow structures from those uncorrelated in the same way as PCD does, since no information of p is used. For example, the second term of (2.14) would stay in the POD spectrum and also exhibit as a dominant mode.

The example shown in figure 2 and 3 illustrates the capability of PCD in extracting flow events from highly noisy data. The temporal signals given in (2.14) are deterministic, we can show in a similar manner that PCD can also effectively extract the observable-correlated flow events when the temporal variation is statistical, such as those exhibited in many turbulent flows. To show this, we construct an artificial one-dimensional flow field

$$u(x, t) = 3s_1(t) \cos x + 2s_2(t) \cos 3x + s_3(t) \cos 6x \exp(-0.1(x - \pi)^2) + 10r(t, x) \quad (2.16)$$

where $s_i(t)$ ($i = 1, 2, 3$) represent three statistical processes. The $s_i(t)$ series are generated by a random number generator with different seeds in MATLAB then filtered using three different 6th-order Butterworth filters. More specifically, $s_1(t)$ is filtered using a bandpass filter with lower and upper cut-off frequencies of $0.2f_s$ and $0.4f_s$, respectively. The $s_2(t)$ and $s_3(t)$ series are filtered using low-pass filters with cut-off frequencies of $0.2f_s$ and $0.15f_s$, respectively. For illustrative purposes, we also added a random noise field that is two orders of magnitude more energetic than $s_3(t)$. Suppose that the observable p is generated by the flow events represented by second and third terms in (2.16), but not by the first, i.e.

$$p(t) = s_2(t - \frac{\pi}{3}) + s_3(t) + 2 \left[s_3(t)^2 - \overline{s_3(t)^2} \right] + 3 \left[s_3(t)^3 - \overline{s_3(t)^3} \right] + r(t) \quad (2.17)$$

Note that because the observable may be non-linearly related with the flow dynamics, we also added in (2.17) two nonlinear terms of $s_3(t)$, as shown by the two bracket terms. Similarly, the observable may be also subject to noise contamination. A statistical random noise $r(t)$, with a uniform distribution over $[-0.5, 0.5]$, is therefore also added. The flow field is again sampled at $f_s = 128/2\pi$ on a uniform spatial mesh of 128 points over the time interval $[0, 2N\pi]$, while p is sampled over $[0, 2(N + 1)\pi]$.

Routine use of the decomposition yields the PCD spectrum and the first two mode vectors, as shown in figure 6(a) and (b), respectively. Clearly, the leading-order mode corresponds to the second term in (2.16), while the second-order mode the third. This

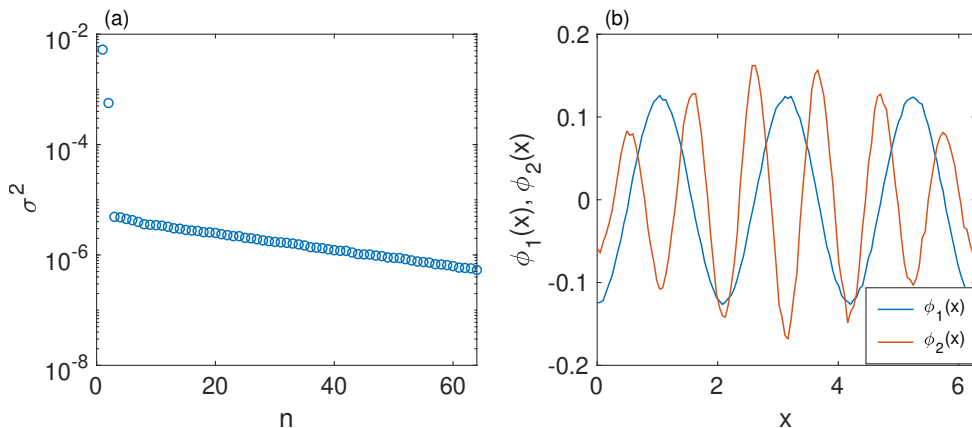


Figure 6: The PCD spectrum (a) and the first and second mode vectors (b). N takes the value of 10000 but 1000 may also be used at the expense of convergence.

can be clearly seen from figure 6(b). It is worth noting the observable also contains the square and cube of $s_3(t)$, but this does not appear to affect the identification of the second mode. Indeed, PCD works by maximizing the correlation between the flow field and the observables, but in general does not limit the two to be linearly correlated. Additionally, the first term of (2.16), due to it being uncorrelated with p , is effectively removed in the PCD spectrum. Other higher-order modes are more than two orders of magnitude lower than the first two. Again, as N increases, these unphysical modes can be further suppressed, while the mode vectors can be resolved more accurately. Note that in this illustrative example, the observable p is also corrupted by the random noise, but PCD continues to work robustly. This shows that PCD can effectively extract flow structures correlated with an observable corrupted by noise.

2.4. Frequency and wavenumber resolution and sampling delay

In section 2.1 we mention that the matrix \mathbf{P} is assumed to have Q rows and each adjacent row is shifted by a fixed time Δt . Moreover, p is sampled temporally behind of u by a time τ_d . In practice, the choice of Q , Δt and τ_d has significant physical implications.

First, we show that Q and Δt determines the maximum and minimum frequencies that can be resolved in the PCD modes, respectively. In particular, Δt determines the maximum frequency similar to the Discrete Fourier Transform (DFT). For example, in section 2.3, the time shift is one sample interval, therefore the maximal frequency that can be resolved is limited by $f_s/2$. Similarly, it can be shown that Q determines the frequency resolution (the minimum frequency). For example, in order to resolve the spectra shown in (2.15), Q must be larger than $Q \geq 2\pi f_s$, i.e. $Q \geq 128$. This is why 128 is used in section 2.3.

Second, the choice of τ_d depends on the causal time delay between p and u . In general, the observable may be the temporally ahead or behind of the flow events depending the

causal relations between the two. For example, if p represents the far-field noise generated by a turbulent flow field u , i.e. u is the source of p , then there must exist a finite time delay between the far-field sound p and the near-field source u due to a finite speed of sound. In this case, p is preferably sampled behind the u in order to capture the physical correlation within a reasonably short sampling duration. Conversely, if p is temporally ahead of u then it must be sampled earlier than u .

In addition to the sampling rate, sampling duration and sampling delay of p , the temporal and spatial sampling of u also have clear physical implications. First, the spatial sampling rate of u has the conventional implication that it determines the maximal spatial wavenumber, whereas the length of the spatial sample determines the minimum wavenumber that can be resolved. The temporal sampling rate of u , however, has a different implication. Strictly speaking, the sampling rate is not to determine the frequency limit, but to ensure the correlation between p and u . In fact, the sampling is not necessarily in the temporal space, but can be in the ensemble space. The sampling rate and duration is to ensure that the correlation converges.

2.5. Connection to POD

As shown in section 2.2, PCD is different from POD in that the decomposition is based on a correlation rather than an energy norm. Mathematically, instead of decomposing the matrix \mathbf{U} , a projection onto \mathbf{P} is performed first. This shows that the decomposition takes into account of the space spanned by \mathbf{P} . POD, however, can be regarded as a special case of PCD when the observable is just an impulse exhibiting no preferences. Mathematically, if $p_{ij} = \delta_{i(N+1-i)}$, $i = 1, 2, \dots, N$, we see that matrix \mathbf{A} is a reversed \mathbf{U} and PCD reduces to POD. Physically, this implies that p contains identical frequency components, therefore exhibit no preferences in the spectral space. Therefore, \mathbf{U} is decomposed into modes ranked purely by their energy.

2.6. Inclusion of multiple observables

In many applications, the appropriate observable is not necessarily limited by one. For example, to examine the dominant flow structures in a subsonic round jet that generate sound at 90° to the jet centerline, the acoustic pressure at any azimuthal position is an appropriate choice due to the azimuthal statistical homogeneity. Including more observables would, as expected, improve the convergence. Suppose the matrix \mathbf{P}_i ($i = 1, 2, 3 \dots L$) can be formed using the i -th observable series according to (2.3), then a straightforward way to include multiple observables is to form the total matrix \mathbf{P} such that

$$\mathbf{P} = [\mathbf{P}_1, \mathbf{P}_2, \mathbf{P}_i \dots \mathbf{P}_L]^T. \quad (2.18)$$

However, it is important to note that although \mathbf{P} has L times as many rows as \mathbf{P}_i , this does not improve the temporal frequency resolution of the decomposition, which is still determined by \mathbf{P}_i . This is similar to padding 0 to a time series before performing DFT.

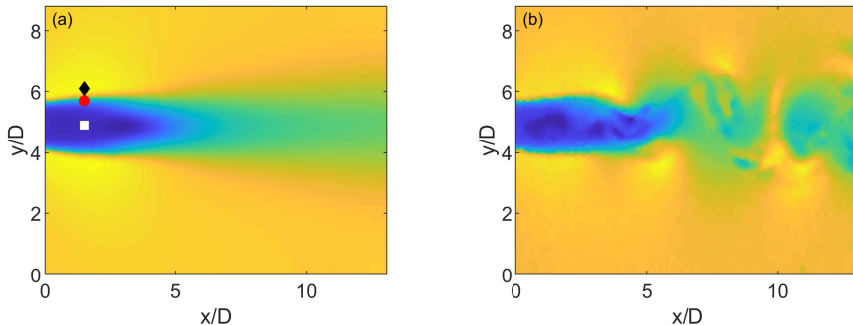


Figure 7: The mean (a) and instantaneous (b) streamwise velocity distributions of the immediately-downstream wake over a cylinder flow (Renn et al. 2023). The black, red and white dots are located at $x/D = 1.5$ but $y/D = 6.1$, $y/D = 5.7$, $y/D = 4.9$, respectively.

No additional temporal resolution is introduced, although the decomposition may yield a smoother spectrum with more singular values. But this may help with the convergence of the resulting PCD modes. For highly complicated flow data with a limited sampling duration, such as those obtained in numerical simulations, including multiple observables is expected to improve the convergence, i.e. reduce the uncertainty or noise of the resulting PCD modes.

3. Applications to experimental and numerical data

Having validated PCD, in section it is used to decompose both experimental and numerical data. We use to two flows to demonstrate the potential applications of PCD.

3.1. Unsteady wake flow over cylinders

The first is an unsteady wake flow over a cylinder measured in experiments. The experiment was performed in a water tunnel using two-dimensional time-resolved Particle Image Velocimetry (PIV) technique. The cylinder had a diameter of $D = 9.53$ mm while the Reynolds number was fixed at 650. The interrogation windows was a rectangle immediately behind an cylinder in the wake and measured $13D \times 9D$ in the streamwise (x) and cross-stream (y) directions respectively. Details of the experiments setup can be found from Renn et al. (2023). The velocity field was sampled at a frequency of around 50 Hz on a mesh of $N_x = 133$ and $N_y = 89$, and in total $N_s = 8250$ snapshots were obtained. The mean and instantaneous streamwise velocity fields are shown in figure 7 for reference. As shown in figure 7, the mean flow exhibits the expected symmetry across the wake, while the instantaneous velocity field shows a clear vortex shedding behaviour behind the cylinder.

The vortex shedding occurring when the Reynolds number exceeds a critical number is one iconic feature of the flow over cylinders. Given its wide applications such as

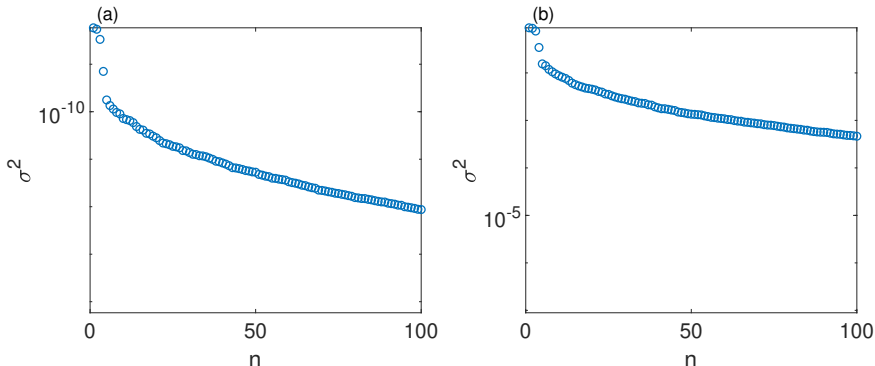


Figure 8: The PCD (a) and POD (b) spectra of the streamwise velocity fluctuations on a $x - y$ plane with the cross-stream velocity fluctuation at $y/D = 5.7$ as the observable.

wind blowing over chimneys and high-rise buildings, its control has attracted significant attention in the fluid mechanics community (Choi et al. 2008). Many techniques exist including both passive and active controls. Earlier studies show that using the feedback signal recorded in the wake, vortex shedding can be successfully suppressed or even eliminated at low Reynolds numbers (Williams and Zhao 1989; Roussopoulos 1993; Park et al. 1994). In designing an closed-loop active control system such as the one in Park et al. (1994), one primary interest is to identify the optimal location to place the feedback sensor. Ideally, the observable, such as the cross-stream velocity, at the feedback sensor location should maintain a strong correlation with the vortex structures shed from the cylinder. PCD may be used to give an initial assessment of the correlation between the sensed signal and the vortex structures.

As an illustration, we choose the observable to be the cross-wake velocity (Park et al. 1994) in the initial shear layer behind the cylinder, for example at $x/D = 0.4$ and $y/D = 5.7$ as shown by the red circular dot in figure 7(a). Using this observable series, the streamwise flow velocity may be decomposed using the PCD method. The time shift τ_d is chosen to be equivalent to $-4/5Q$ samples long while Q is chosen to be $1/3N_s$. Figure 8(a) and (b) shows the PCD and POD spectra, respectively. Clearly, both PCD and POD capture the dominant vortex shedding behaviour, and the two identical singular values reflects a convecting behaviour of the shed vortices. Figures 9 and 10 show the corresponding first three PCD and POD modes and their corresponding Power Spectral Density (PSD), respectively. Clearly the first two vortex shedding modes from both PCD and POD are virtually identical, which can be seen from both the mode shape and their corresponding PSD spectra. The PCD spectrum shows a slightly smaller singular value for the third mode, which is somewhat more symmetric, whereas the similar mode resulting from POD obtains a similar singular value compared to the leading-order mode. This suggests that although this mode carries one of the largest energy but it is slightly less correlated with the cross-stream velocity fluctuation at $x/D = 1.5$ and $y/D = 5.7$.

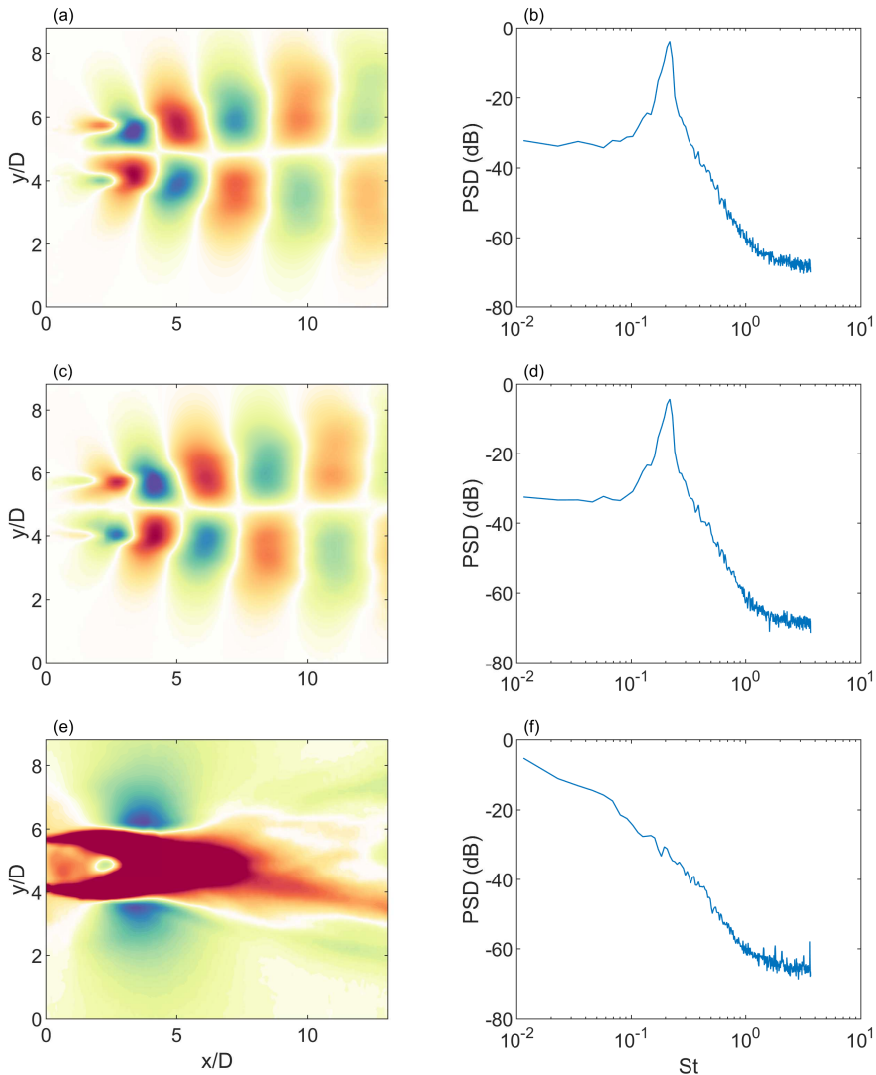


Figure 9: The first 3 PCD modes (a-b-e) and PSD (b-d-f) of their corresponding temporal variation coefficients; mode 1 (a-b), mode 2 (c-d) and mode 3 (e-f);

If we keep $x/D = 1.5$ but move the observable position further away from the shear layer, for example to $y/D = 4.9$ and $y/D = 6.1$, respectively, these three modes can still be identified using PCD, but their relative singular values changed significantly, as shown in figure 11. This implies that these modes correlate differently to different observables. Evidently, the first and second order modes in figure 11(a) represent the vortex shedding modes. Their mode shapes are similar to those shown in figure 9(a) and (b) so we omit a repetitive presentation. However, it is important to note that these singular values are much larger compared to those shown figure 10(a), suggesting they are more correlated with the observable. More importantly, the third singular value drops rapidly, almost

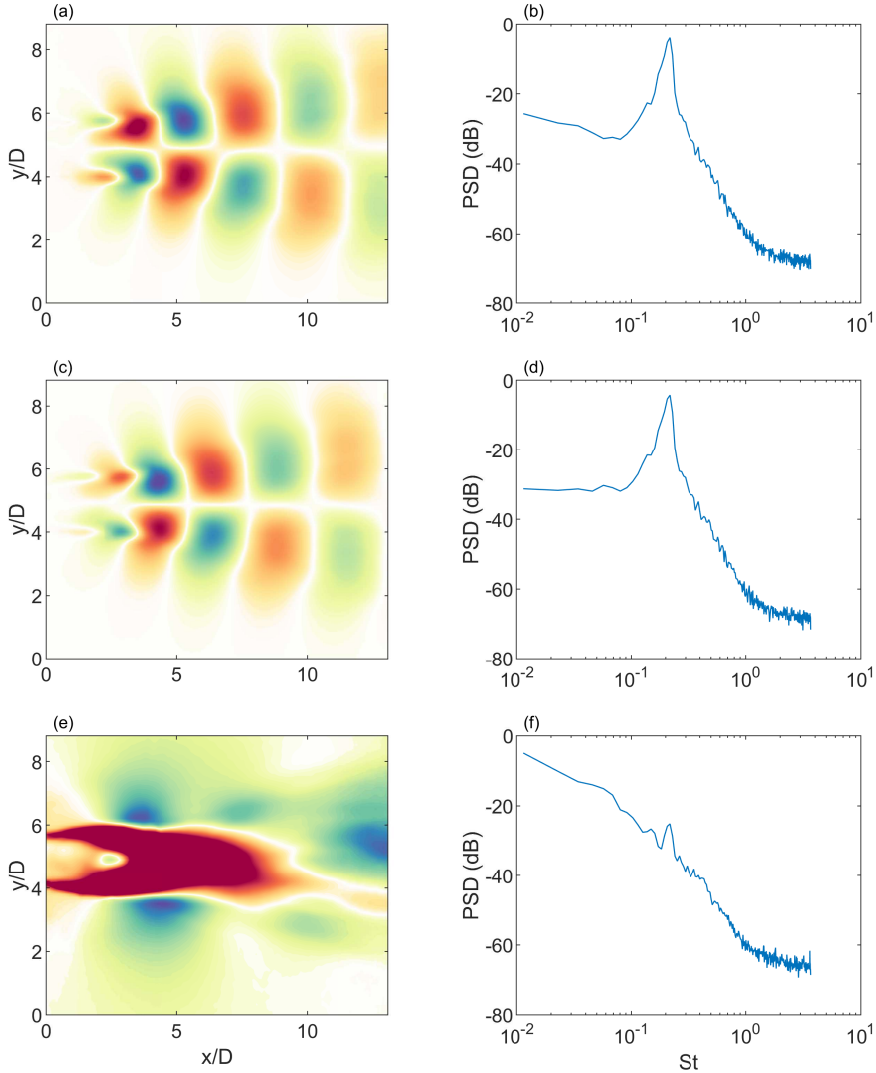


Figure 10: The first 3 POD modes (a-b-e) and PSD (b-d-f) of their corresponding temporal variation coefficients; mode 1 (a-b), mode 2 (c-d) and mode 3 (e-f);

one order of magnitude weaker than the leading-order mode. From the feedback control point of view, this would be a good candidate for placing the feedback sensor own to its higher correlation with our interested flow events and simultaneously a higher SNR. Figure 11(b) shows that the singular values corresponding to the vortex shedding modes are slightly lower than those shown in figure 9(a) with an even stronger leading-order non-shedding mode. Consequently, this may not be an ideal position for placing the feedback sensor. This may be why the wake centerline was used to place the feedback sensors in [Park et al. \(1994\)](#).

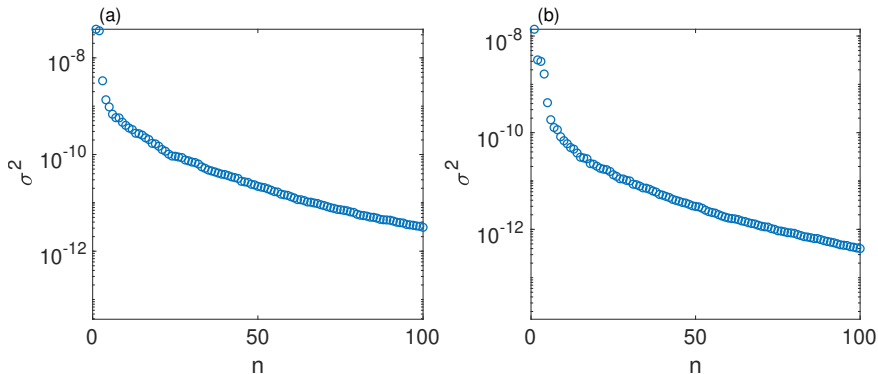


Figure 11: The PCD spectra of the streamwise velocity fluctuations when the observable is located at $y/D = 4.9$ (a) and $y/D = 6.1$ (b), respectively.

3.2. Turbulent subsonic round jets

In this section, we apply PCD to a numerical dataset of a turbulent subsonic round jet. The mechanism of sound generation by turbulence remains as an open question in jet aeroacoustics. Lighthill's acoustic analogy (Lighthill 1952, 1954) provides a rational basis on which one can understand the scaling of jet noise, and with the help of source models, approximately predict jet noise. However, it is well-established that Lighthill's quadrupoles are not physical sources. The very question of how sound is generated by turbulence is still an open question. Using far-field sound as the observable, PCD would be particularly suitable to extract the those flow features that are acoustically relevant. Considering that directly resolving far-field sound is expensive in numerical simulations, the FW-H method (Williams and Hawkings 1969) or Lighthill's acoustic analogy in the temporal domain may be used. However, to avoid the error introduced in these approaches, in this illustration example we purposely choose a resolved near-field pressure fluctuation at an interior point within the computational domain. Although not being far-field sound, the near-field pressure fluctuations are indeed generated by the structures within the jet, and hence would also be suitable for demonstrating the usage of PCD. Furthermore, the near-field pressure fluctuations are crucial in determining the installed jet noise (Lyu et al. 2017), therefore its modelling and control has practical engineering applications. In fact, it was shown that when a wing is placed in the vicinity of a jet's near field, the near-field pressure is directly scattered into sound in a linear manner.

The numerical data is extracted from an earlier work (Lyu et al. 2017), where an LES simulation of a subsonic round jet was performed. Only a slice data on one azimuthal plane is used but should be sufficient for illustration purposes. The jet Mach number is $M_j = 0.5$ while the nozzle diameter D is 2 inches. The computational domain is axisymmetric, with the streamwise coordinate x extending from 0 to $20D$ and lateral coordinate r extending to $4D$. Considering the limited radial extent, we choose the near-

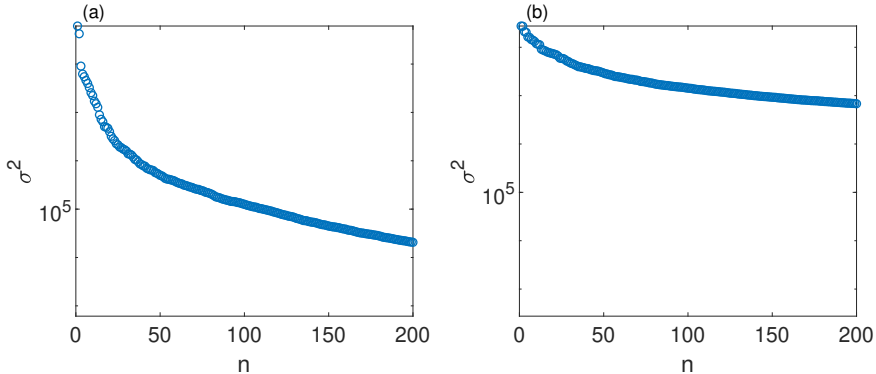


Figure 12: The PCD (a) and POD (b) spectra of the unsteady pressure field on a $x - r$ plane. The PCD spectrum shows a clear low-rank behaviour compared to POD.

field pressure fluctuation at $x/D = 10$ and $r/D = 4$ as the observable. At this close distance, the observable is likely to include both the acoustic and hydrodynamic pressure fluctuations. The x and r coordinates are discretized using 512 and 97 points, respectively. The pressure field within the flow is sampled at a frequency of $4U_j/D$ for a duration of $200U_j/D$, where U_j is the jet exit velocity. The acoustic pressure p , on the other hand, is sampled at the same frequency for a longer duration of $280U_j/D$. Due to the short distance between the flow field and the near-field pressure fluctuations, we choose the time delay τ_d to be 0.

With the procedure described in section 2.1, the PCD spectrum is shown in figure 12. Also shown is the POD spectrum to facilitate a direct comparison. Only the first 200 singular values are shown. Compared to POD, the PCD spectrum exhibits a more rapid decay as the mode number n increases. In particular, at small mode numbers PCD spectrum shows a clear low-rank behaviour. The first two modes are almost one order of magnitude stronger than higher-order modes. This is in direct contrast to POD spectrum, where the low-rank behaviour is not pronounced. This can be understood from Figure 14 and 15, where first 6 PCD and POD modes $\phi_k(\mathbf{x})$ and the corresponding PSD of their temporal expansion coefficients $a_k(t)$ are shown, respectively. Clearly, the first two PCD modes are large flow structures exhibiting relatively low-frequency behaviour, whereas the leading-order POD modes have much shorter scales with a well-known dominant frequency at around $St = 0.3$, where St is the Strouhal number defined using U_j and D . Since the observer is located at $x/D = 10$ and $r/D = 4$, the pressure fluctuations inevitably include the signatures of the downstream large coherent structures. The nearly identical first two singular values shown in figure 12 and similar mode shapes show in figure 14 indicate the convection behaviour of this large structure. PCD decomposition can take this into consideration and yield an observable-relevant low-frequency fluctuation mode. The leading-order POD modes, on the other hand, are ranked only by the fluctuation energy, therefore are not as relevant as the PCD modes.

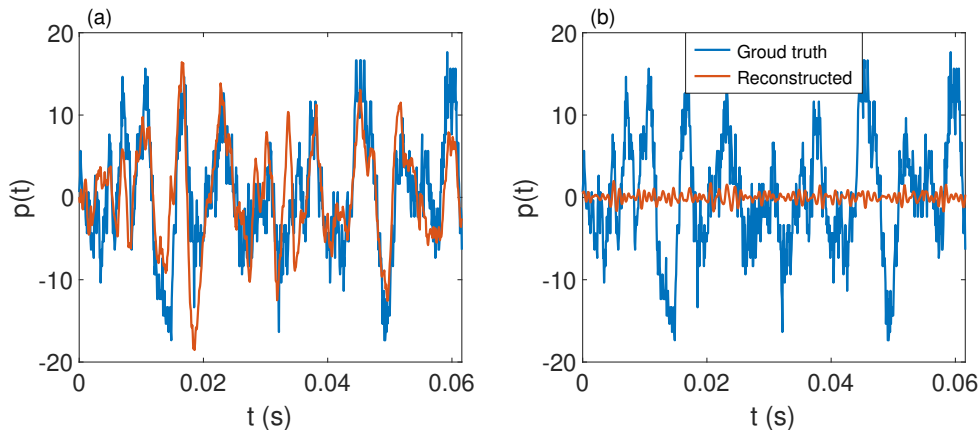


Figure 13: The reconstructed pressure fluctuations at the observable location using the first 2 PCD (a) and POD modes (b), respectively.

Note that the singular value represents a measure of the correlation in L_2 norm, and therefore is in general not equal to the energy of the PCD modes contained in the flow. Nevertheless, since the decomposition targets more at the observable, we expect that it can reconstruct the pressure fluctuations at the observable position using much fewer modes, i.e. the expansion in (2.6) converges more rapidly. This is indeed the case, as shown in figure 13, where only the first two PCD and POD modes are included to calculate the reconstructed pressure fluctuations at the observable position, respectively. The reconstructed pressure fluctuations are then compared with the ground truth to evaluate the rate of convergence. As can be seen from figure 13(a), using two PCD modes can yield a very good reconstruction. In fact, more than 80% of the energy of $p(t)$ is recovered. On the other hand, from figure 13(b) we see that little energy is recovered from the first two POD modes. This further confirms the low-rank behaviour shown in figure 12. Note that in this application we use the pressure field as the flow u , whereas in general a combined velocity and pressure field may be used. We can show that a similar low-rank behaviour may also be obtained when a combination of velocity and pressure fluctuations are used in PCD.

At large mode numbers, the PCD spectrum shows a steeper decay and the higher-order modes tend to have increasingly short scales together with higher frequencies, as shown in figure 12 and 14, respectively. Note that the singular values represent the correlation energy between the PCD modes and the observable, therefore the decay of the singular values is determined by both the energy of the flow and the observable and the coherence decay between them. Therefore, the steeper PCD spectrum appears to suggest that although the pressure fluctuations consist of energetic structures of various scales, they may not be equivalently important in contributing the observable, therefore the coherence between the two may decrease rapidly. On the other hand, the POD spectrum decays much more slowly, and as the mode number increases the POD mode starts to

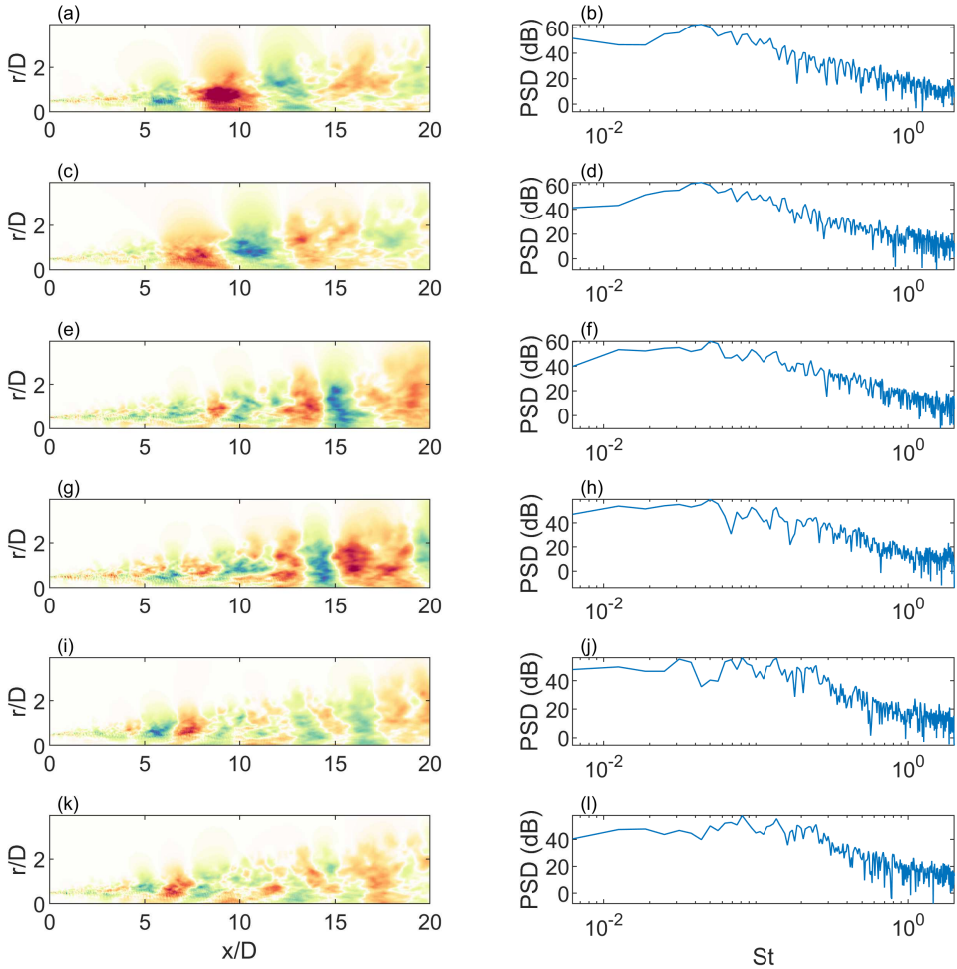


Figure 14: The first 6 PCD modes (a-c-e-g-i-k) and PSD (b-d-f-h-j-l) of their corresponding time variation coefficients; mode 1 (a-b), mode 2 (c-d), mode 3 (e-f), mode 4 (g-h), mode 5 (i-j), and mode 6 (k-l). As the mode number increases the scales become shorter with more high-frequency components.

capture more downstream large structures with more low-frequency content, as can be shown in figure 15. The fact the POD spectrum decays more slowly can be attributed to the fact that POD spectrum is determined only by the energy of flow, therefore does not include its coherence with the observable.

Figure 12 shows that using the near-field observable as a reference, PCD can effectively extract the flow structures that are most relevant to determining the near-field pressure fluctuations. Using two modes can recover more than 80% energy of the near-field pressure fluctuations. POD, however, does not have this observable exclusiveness, and therefore yields a decomposition that results in a slow reconstruction of the near-field pressure.

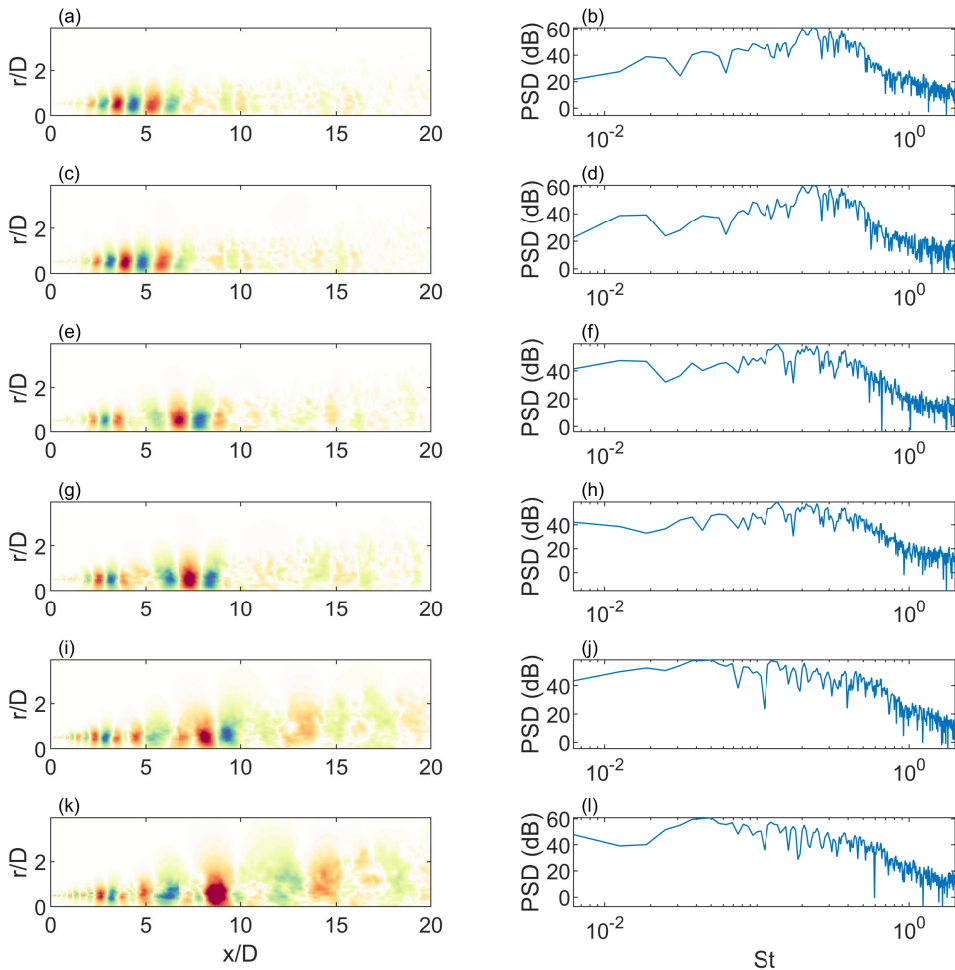


Figure 15: The first 6 POD modes (a-c-e-g-i-k) and PSD (b-d-f-h-j-l) of their corresponding time variation coefficients; mode 1 (a-b), mode 2 (c-d), mode 3 (e-f), mode 4 (g-h), mode 5 (i-j), and mode 6 (k-l). As the mode number increases the downstream scales become larger with more low-frequency components.

Figure 14 shows that each PCD mode corresponds to a unique temporal variation. Unlike the Fourier analysis, each of these temporal variation is spectrally broadband. In essence, PCD decomposition works as a special spectral transform of the flow based on its correlation with the observable. Note, however, the sampling duration is limited in this simulation, and further analysis using longer samples is needed for better statistical convergence. In addition, due to current data availability, we only decompose the near-filed pressure, and it would be interesting to apply this technique to extract acoustically dominant flow features in the future studies.

4. Conclusion

A new data-driven method is proposed in this paper to decompose flow into modes ranked by their correlation energy with an observable. The new method is based on the singular value decomposition of a correlation matrix between the flow and a given observable. The new method is validated for both deterministic and statistical flow events. First, the results show that PCD can effectively extract the observable-correlated flow features while suppressing those uncorrelated in both cases. PCD therefore results in more low-rank spectra compared to POD. Second, PCD can effectively extract those observable-correlated flow structures even under a very low SNR. This is especially suitable for flow diagnosis of energetically weak observable, such as identifying the aeroacoustic source structures within a complex flow. Third, numerical validation shows that the convergence of the PCD continues to improve for longer samples. Therefore PCD is particularly suitable for experimental data where long samples are more conveniently obtained. Lastly, as no linearity is assumed, PCD is capable of extracting nonlinear flow events similar to POD, provided non-negligible correlation exists between the flow and the observable.

The new method is subsequently applied to analyse the unsteady vortex shedding behind a cylinder at a Reynolds number of 650. It shows that similar modes to POD can be robustly identified, but their strengths depend crucially on the observable and its locations, suggesting that these modes correlate differently with different observables. In the subsequent example, PCD is used to decompose the unsteady pressure field of a turbulent subsonic jet using a near-field pressure fluctuation as the observable. Results show that PCD results in a steeper spectrum compared to POD. In particular, the PCD spectrum exhibits a clear low-rank behaviour and the corresponding modes correspond to the large coherent flow structures that convect downstream. The first two PCD modes effectively recover 80% of the energy of the near-field pressure fluctuations, while the first two POD modes only recover negligible energy. Note, however, the sampling duration of the numerical database is very limited, therefore a longer sampling duration is needed for more accurate diagnosis. This, together with far-field noise diagnosis, forms our some future work.

Acknowledgements

The author wishes to gratefully thank Dr. Cong Wang and his collaborators for agreeing to user their PIV data on cylinder wakes. The author wishes to thank Dr. I. Naqavi who performed the LES simulations in our last collaborative publication (Lyu et al. 2017), from which part of the data is extracted and reused. The author also wishes to gratefully acknowledge the central research fund under the grant number of 8206100355.

- N. Aubry. On the hidden beauty of the proper orthogonal decomposition. *Theoretical and Computational Fluid Dynamics*, 2:339–352, 1991.
- G. Berkooz, P. Holmes, and J. L. Lumley. The proper orthogonal decomposition in the analysis of turbulent flow. *Annual Review of Fluid Mechanics*, 25:539–575, 1993.
- H. Choi, W. Jeon, and J. Kim. Control of flow over a bluff body. *Annual Review of Fluid Mechanics*, 40:113–139, 2008.
- M. J. Colbrook, L. J. Ayton, and M. Szöke. Residual dynamic mode decomposition: robust and verified Koopmanism. *Journal of Fluid Mechanics*, 955(A21), 2023.
- B. Farrell and J. Ioannou. Stochastic forcing of the linearized Navvier-Stokes equations. *Physics of Fluids*, 5(11):2600–2609, 1993.
- J. B. Freund and T. Colonius. Turbulence and sound-field POD analysis of a turbulent jet. *International Journal of Aeroacoustics*, 8(4):337–354, 2009.
- J. Jeun, J. W. Nichols, and M. R. Jovanović. Input-output analysis of high-speed axisymmetric isothermal jet noise. *Physics of Fluids*, 28(4):047101, 2016.
- M. R. Jovanović. From bypass transition to flow control and data-driven turbulence modeling: an input-output viewpoint. *Annual Review of Mechanics*, 53:311–45, 2021.
- M. J. Lighthill. On sound generated aerodynamically. I. General theory. *Proceedings of the Royal Society A: Mathematical, Physical and Engineering Sciences*, 211(1107):564–587, Mar 1952.
- M. J. Lighthill. On sound generated aerodynamically. II. Turbulence as a source of sound. *Proceedings of the Royal Society A: Mathematical, Physical and Engineering Sciences*, 222:1–32, Feb 1954.
- J. L. Lumley. The structure of inhomogeneous turbulence. *Atmospheric Turbulence and Wave Propagation*, pages 166–178, 1967. ed. AM Yaglom, VI Tatarsky, Nauka, Moscow.
- J. L. Lumley. *Stochastic tools in turbulence*. Academic Press, 1970.
- B. Lyu, A. Dowling, and I. Naqavi. Prediction of installed jet noise. *Journal of Fluid Mechanics*, 811:234–268, 2017.
- B. J. Mckeon. A critical-layer framework for turbulent pip flow. *Journal of Fluid Mechanics*, 658:336–382, 2010.
- D. S. Park, D. M. Ladd, and E. W. Hendricks. Feedback control of von Karman vortex shedding behind a circular cylinder at low Reynolds numbers. *Physics of Fluids*, 6(2390), 1994.
- P. I. Renn, C. Wang, S. Lale, Z. Li, A. Anandkumar, and M. Gharib. Forecasting subcritical cylinder wakes with Fourier Neural Operators. *ArXiv*, 2301:08290, 2023.
- K. Roussopoulos. Feedback control of vortex shedding at low Reynolds numbers. *Journal of Fluid Mechanics*, 248(267-296), 1993.
- P. Schmid. Dynamic mode decomposition of numerical and experimental data. *Journal of Fluid Mechanics*, 656:5–28, 2010.
- P. Schmid. Dynamic mode decomposition and its variants. *Annual Review of Fluid Mechanics*, 54:225–254, 2022.
- O. T. Schmidt, A. Towne, G. Rigas, T. Colonius, and G. A. Brés. Spectral analysis of jet turbulence. *Journal of Fluid Mechanics*, 855:953–982, 2018.
- L. Sirovich. Turbulence and the dynamics of coherent structures, Parts I-III. *Quarterly of Applied Mathematics*, 45(3):561–590, 1987.
- K. Taira, S. Brunton, S. T. M. Dawon, C. W. Rowley, T. Colonius, B. J. Mckeon, O. T. Schmidt, S. Gordeyev, V. Theofilis, and L. S. Ukeiley. Modal analysis of fluid flows: an overview. *AIAA Journal*, 55:4013–4041, 2017.

- A. Towne, O. T. Schmidt, and T. Colonius. Spectral proper orthogonal decomposition and its relationship to dynamic mode decomposition and resolvent analysis. *Journal of Fluid Mechanics*, 847:821–867, 2018.
- L. N. Trefethen, A. E. Trefethen, S. C. Reddy, and T. A. Driscoll. Hydrodynamic stability without eigenvalues. *Science*, 261(5121):578–584, 1993.
- J. E. Williams and B. C. Zhao. The active control of vortex shedding. *Journal of Fluids and structures*, 3:115–122, 1989.
- J. E. F. Williams and D. L. Hawkings. Sound generation by turbulence and surfaces in arbitrary motion. *Philosophical Transaction of the Royal Society of London. Series A, Mathematical and Physical Sciences*, 264:321–342, 1969.
- M. O. Williams, I. G. Kevrekidis, and C. W. Rowley. A data-driven approximation of the Koopman operator: extending dynamic mode decomposition. *Journal of Nonlinear Science*, 25:1307–1346, 2015.